Chemical Data Collections 40 (2022) 100884

Contents lists available at ScienceDirect

Chemical Data Collections

journal homepage: www.elsevier.com/locate/cdc

Data Article

Fused filament fabrication and water contact angle anisotropy: The effect of layer height and raster width on the wettability of 3D printed polylactic acid parts

Jack Kingman, Marcus K. Dymond *

Chemistry Research and Enterprise Group, University of Brighton, Brighton BN2 4GL, United Kingdom

ARTICLE INFO

Keywords:
3D printing
Additive manufacturing
Fused filament fabrication
Water contact angles
Contact angle anisotropy

ABSTRACT

Herein water contact angles obtained on 3D printed surfaces of polylactic acid, manufactured by fused filament fabrication, are measured and collated. Data are contained within the article and show that 3D printed parts exhibit considerable water contact angle anisotropy. A series of studies are presented whereby the fabricated layer height of the 3D print and the raster width of the print are varied. In general, we observe that contact angle anisotropy is greatest for larger z-layer heights and wider raster widths. The effect of different build platform surfaces is also studied, suggesting that for applications, where 3D prints are to be used in an aqueous environment, altering raster width and layer height provides a useful way to tune the wettability of the final 3D printed part. Furthermore, our results suggest end users should be cautious when changing the print settings of devices in wettable environments, since very different surface behaviors, which may impact reproducibility, can result.

1. Rationale

In recent years, the affordability of fused filament fabrication (FFF) 3D printers has made it possible to explore the potential of additive manufacturing within the chemical and biological sciences. A wide range of applications have been investigated such as FFF reactionware [1–4], customized spectroscopic equipment [5–9], biosensors [10–13] and microfluidic devices [14–16].

One of the advantages of FFF 3D printing is that these printers can print a range of different materials, which broadens the range of potential applications. However, before FFF 3D printing can be routinely incorporated into biological and chemical applications, which typically feature fluid interacting interfaces, several challenges remain. For example, the way that FFF prints are constructed, through multiple extruded layers, makes it difficult to reproducibly construct leak-free 3D prints. Post-print treatment by immersion in organic solvents [5,17] or by coating with epoxy resin [10] has been shown to be an effective way to ensure watertight FFF prints, although these approaches can impact the dimensional accuracy of the print. One of the other challenges of FFF 3D printing is that the printing process, which utilizes different extrusion speeds, travel speeds, printing patterns, nozzle diameters, print orientations, tool paths and layer heights, to construct the 3D print, gives rise to different degrees of surface roughness in the final design [18–20]. Surface roughness can impact the utility of 3D prints in a number of different ways, such as through its effect on dimensional accuracy [19], the ease of gripping the final 3D printed object [18], and the wettability of surfaces [17], although it should be noted that wettability is dependent on the material chemistry but can be modified by surface treatment.

* Corresponding author.
E-mail address: M.Dymond@brighton.ac.uk (M.K. Dymond).

https://doi.org/10.1016/j.cdc.2022.100884
Received 20 August 2021; Received in revised form 6 May 2022; Accepted 16 May 2022
Available online 18 May 2022

Equilibrium contact angle theory was established by Young [21] and refers to a system where a liquid droplet rests on an ideal solid (i.e. a perfectly smooth, non-reactive, chemically homogenous, insoluble rigid surface). Contact angles measured on these ideal surfaces are termed intrinsic contact angles, whilst actual contact angles are the contact angle of 'non-ideal' surfaces and apparent contact angles are the angle measured [22]. One of the most difficult aspects of contact angle analysis is the surface roughness, which can have a large impact on the apparent contact angle. This occurs because, as the surface roughness increases, the number of favorable (or unfavorable) intermolecular interactions increases thus deforming the liquid droplet. However, the size of the surface features also impacts the contact angle through the phenomena of full and partial wetting. In full wetting all the surface roughness features are accessible to the liquid, the Wenzel model, where the apparent contact angle is a function of the roughness ratio (actual surface area: to apparent surface area)[23]. In partial wetting, described by the Cassie-Baxter model, the surface is heterogeneous and the roughness is a function of the fraction of the solid surface in contact with the liquid [23]. Depending on whether the surface is hydrophobic or hydrophilic and whether full or partial wetting is occurring, a wide range of contact angles can be observed [24].

By exploring the relationship between water contact angles and different FFF settings we hope to enable researchers to tune surface wettability of 3D prints. We chose to use PLA because this material is probably the most widely accessible filament and basic FFF printer models can print it, since a heated build platform is not required for print adhesion. Furthermore, PLA is a biodegradable polymer [25] that can be produced from plant derived starting materials [26], making it a sustainable choice with low environmental impact [25]. There are several topical areas of 3D printing that may benefit from this knowledge and some previous work in this area has been undertaken, such that layer height and raster angle are known to impact the wettability of 3D printed PLA parts [27,28]. In this study, we chose to characterize all surfaces of a simple 3D printed cube at a range of layer heights and raster widths greater than any currently published. This information is important because surface wettability is a factor in determining cellular [29] and protein [30] adhesion to surfaces, which impacts on the efficacy of FFF implants [31] and bioprinting or tissue engineering applications [32–35]. Similarly, there is interest in 3D printed solid catalysts [36] or 3D printed supports for catalysts [37] and it is well established that surface wettability can impact catalytic activity [38]. Finally, the behavior of microfluidic systems is also impacted by surface wettability [39] and there is much interest in 3D printing microfluidic systems, as reviewed [40].

2. Procedure

2.1. 3D printing protocols

3D printing was performed on an Ultimaker 2Go 3D printer (Ultimaker, NL), using PLA filament (natural, 2.85 mm, Ultimaker, NL) equipped with a 0.4 mm extruder nozzle. The build platform of the 3D printer was levelled according to the standard calibration procedure using a metal 'feeler gauge' of 0.15 mm to obtain a reproducible height between the build platform and extruder nozzle. 3D print designs were prepared in Autodesk 123D Design, sliced using Ultimaker Cura 4.0.0 and printed in the center of the build platform. Print settings for PLA were: extruder temperature (200°C); build platform (ambient); retraction distance (6.5 mm), retraction speed (25 mm/s); fan speed (100%), print speed (60 mm/s); infill density (20 %); wall thickness (0.8 mm); top/ bottom thickness (0.8 mm); build plate adhesion type (brim) and brim width (20 mm). Parameters such as layer height (z-layer height), line width (raster width) were varied depending on the experiment. A full list of the print parameters used is provided as Supporting Information. Prior to printing, the build platform was covered with blue masking tape (Blue Tape, Eurocel) or polyimide tape (Kapton tape, Aixin). All contact angle measurements were performed on a 3D printed cuboid (10 × 10 × 10 mm) using the experimental settings detailed in Sections 2.2 to 2.5.

2.2. Measurement of water contact angles on 3D printed surfaces

Contact angle measurements were obtained using a contact angle goniometer (OCA15 plus, firmware version SCA20). Before measurements were taken, syringes (Hamilton microliter syringes, DS 500/GT, GasTight 500 μl) were rinsed three times with pure water (18.2 mΩ water, obtained using a Purelab Option DV25 (ELGA) reverse osmosis system). Experiments were performed using a water droplet (5.0 μl, 18.2 mΩ water, Purelab Option DV25 (ELGA) reverse osmosis system), dispensed at a rate of 0.50 μl/s, from the microliter syringe fixed to the goniometer, onto the 3D printed surface. 3D prints were stored in an airtight bag after printing and surfaces were wiped using Kimwipes (Kimberly Clark) before measurements were made. Images of sessile water droplets were taken after 10 seconds at ambient temperature and internal contact angles were calculated as the average of both the right and left sides of the drop. The 'intrinsic' water contact angle of PLA was determined by collecting extruded filament directly onto glass microscope slide, measuring the contact angle on the smooth surface that was in contact with the glass. Data show the mean average ± standard deviation of the contact angle of 3 different water drops on 3 separate 3D prints. Statistical analyses were performed in GraphPad Prism using one wat ANOVA with a 95% confidence limit.

2.3. Experiments to determine the effect of z-layer height on water contact angles

Starting from the standard 3D printing settings described in section 2.1, 3D prints were manufactured at 0.05, 0.10, 0.15, 0.20 and 0.25 mm z-layer heights, with a raster width of 0.4 mm. Contact angle measurements were performed on three different prints, manufactured at each layer height specified and on all surfaces of the cube design. Water drops were placed in the center of the surface under study. Data are reported as the mean average plus/ minus the standard deviation of the mean.

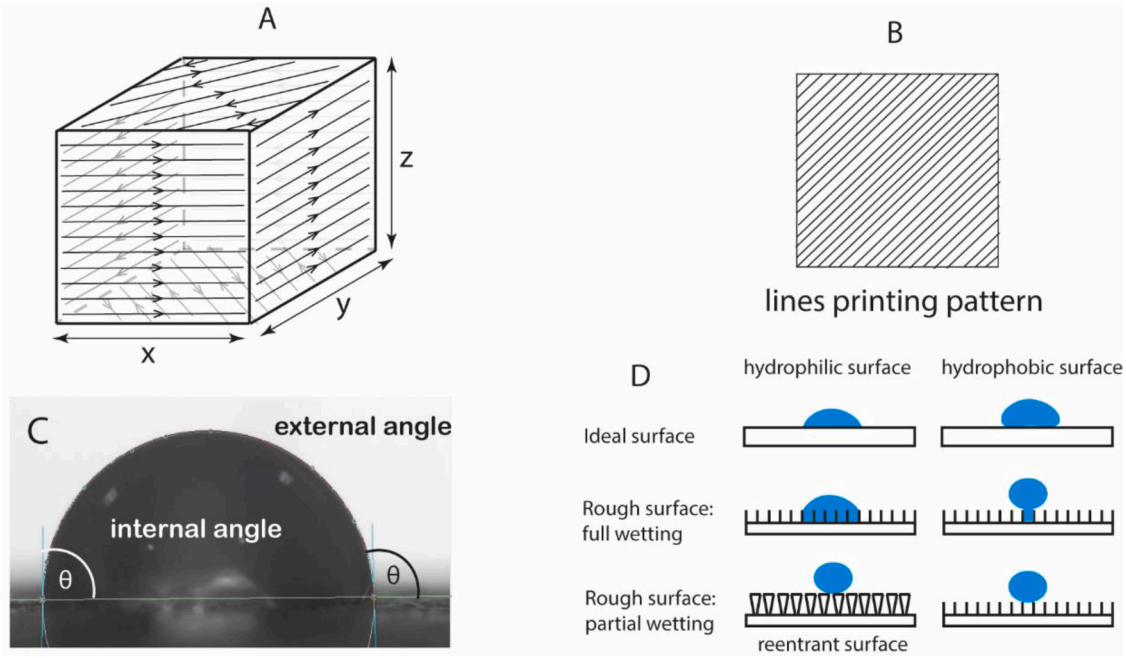

Fig. 1. Definition of terms used to describe the 3D printed object, 3D printing methodology and contact angles. Fig. 1A defines the surface position on the 3D print where the water contact angle was measured and the x, y and z print dimensions relative to this, where z is the build direction. Arrows show the direction of the extruder head or 'tool path'. Fig. 1B the lines printing pattern finish, viewed from above. Fig. 1C shows an example contact angle of water on PLA. Fig. 1D overviews the different ways that water contact angles can be affected by ideal and rough surfaces [23,24].

Table 1
Water contact angles on surfaces with lines printing pattern: effect of z-layer height [a]

Internal Contact Angle mean ± SD (°)								
z-layer height (mm)	Parallel to tool path			Parallel to build direction				
	Top Face	Bottom Face (Blu Tape)	Bottom Face (Kapton Tape)	Front Face (1)	Rear Face (2)	Left Face (3)	Right Face (4)	Average Sides
0.05	84.3 ± 3.0	76.1 ± 11.2	81.3 ± 3.6	78.0 ± 5.5	82.2 ± 2.2	75.9 ± 4.0	76.9 ± 0.4	78.2 ± 3.0
0.10	75.6 ± 3.8	73.9 ± 3.1	84.7 ± 0.3	77.7 ± 7.9	74 ± 12.2	75.8 ± 3.5	72 ± 6.3	74.8 ± 1.9
0.15	72.9 ± 2.5	80.9 ± 3.4	81.1 ± 0.9	79.6 ± 1.0	80 ± 2.7	76.1 ± 1.2	79.5 ± 2.1	78.8 ± 1.0
0.20	75.8 ± 3.9	81.1 ± 6.4	78.3 ± 7.4	76.4 ± 4.9	75.4 ± 2.1	77.0 ± 3.4	76.4 ± 1.7	76.3 ± 2.1
0.25	71.4 ± 5.6	86.0 ± 4.7	77.8 ± 1.1	76.0 ± 5.4	73.6 ± 3.2	79.2 ± 4.1	77.3 ± 1.7	76.5 ± 1.3
z-layer height (mm)	**Perpendicular to tool path**			**Perpendicular to build direction**				
	Top Face	**Bottom Face (Blu Tape)**	**Bottom Face (Kapton Tape)**	**Front Face (1)**	**Rear Face (2)**	**Left Face (3)**	**Right Face (4)**	**Average Sides**
0.05	72.9 ± 6.2	72.3 ± 0.5	112.6 ± 8.1	88.4 ± 9.7	97.4 ± 13.0	95.9 ± 0.9	89.7 ± 18.5	92.8 ± 8.8
0.10	89.4 ± 5.8	84.8 ± 1.1	106.5 ± 6.3	92.1 ± 12.8	90.0 ± 6.4	91.0 ± 4.9	91.2 ± 9.1	91.1 ± 5.3
0.15	83.1 ± 2.7	79.4 ± 3.72	107.5 ± 2.7	102.9 ± 6.8	103.0 ± 11.4	98.3 ± 5.7	100.1 ± 5.1	101.1 ± 3.0
0.20	91.9 ± 6.7	92.1 ± 2.6	100.6 ± 5.7	105.6 ± 4.4	103 ± 2.1	105.6 ± 13.3	111.5 ± 8.1	106.4 ± 3.6
0.25	105.8 ± 3.3	80.3 ± 2.3	91.4 ± 5.3	110.7 ± 5.4	105.6 ± 8.2	108.5 ± 8.9	109.2 ± 5.2	108.5 ± 4.0

[a] data were obtained on cubes printed at a raster width of 0.4 mm.

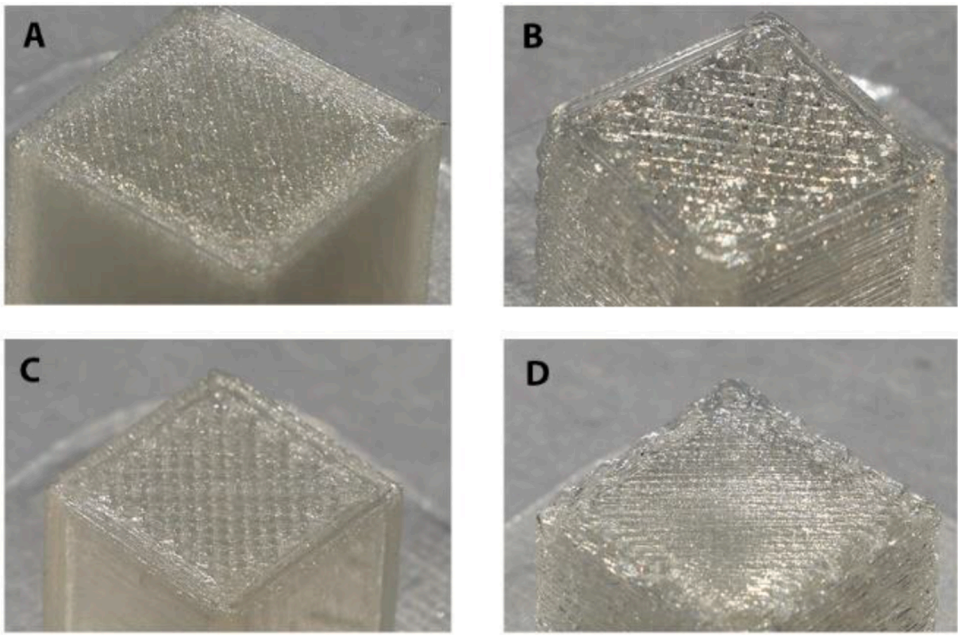

Fig. 2. Examples of 3D printed surfaces at different layer heights and raster widths. Fig 2A shows 0.05 mm z-layer height and 0.20 mm raster width. Fig. 2B shows 0.25 mm z-layer height and 0.60 mm raster width. Fig 2C shows 0.05 mm z-layer height and 0.60 mm raster width. Fig 2D shows 0.25 mm z-layer height and 0.20 mm raster width.

2.4. Experiments to determine the effect of raster width on water contact angles

Starting from the standard 3D printing settings described in section 2.1, 3D prints were manufactured at 0.05, 0.10, 0.15, 0.20, 0.25, 0.30, 0.35, 0.45, 0.50, 0.55 and 0.60 mm raster widths. For each set of raster widths 3D prints with z-layer heights of 0.05, 0.10, 0.15, 0.20 and 0.25 mm were constructed. Contact angle measurements were performed in the center on the top surface of three different prints, manufactured at each raster width and layer height specified. Data are reported as the mean average plus/ minus the standard deviation of the mean.

2.5. Experimental definitions and terminology

Fig. 1 gives a definition of 3D printing terminology relevant to this study and background information on water contact angles.

3. Data, value and validation

3.1. The effect of z-layer height on the wettability of 3D printed surfaces

Initially we determined the 'intrinsic' water contact angle of the PLA filament used in this study, by allowing the extruded filament to pool on a glass microscope slide. The internal contact angle on the smooth surface that had been in contact with glass was 70.7 ± 2.4°, which is its value under full wetting. No contact angle anisotropy was observed. The asymmetric nature of 3D printing patterns makes the surface roughness of the material direction-dependent [20]. For example, previous work with FFF and polyethylene terephthalate glycol (PETG) demonstrated that the surface roughness perpendicular to the lines of the printing pattern is significantly higher than surface roughness parallel to the lines of the printing pattern [41]. Similarly, studies have demonstrated anisotropy in the water contact angles of 3D prints when measured parallel and perpendicular to the tool path or build direction [20,24]. Table 1 shows the different internal contact angles of water we obtained parallel and perpendicular to the tool path, when z-layer height is changed using the lines surface pattern (Fig. 1B). Fig. 2 provides example images of 3D printed cubes at different print settings, where clear differences in the surface texture can be observed.

As shown in Table 1, water contact angles on the top surface range from *circa* 71.4 ± 5.6 to 84.3 ± 3.0 °, when measured parallel to the tool path, which is consistent with full wetting of PLA [42]. Internal water contact angles, measured perpendicular to the tool path, increase from 72.9 ± 6.2 ° at a layer height of 0.05 mm to 105.8 ± 3.3 ° at a layer height of 0.25 mm. These values are consistent with full wetting of PLA, at small layer heights but demonstrate that as layer height increases, the surface behaves under conditions of partial wetting. The intrinsic contact angle we determined as 70.7 ± 2.4° is comparable to some of the values we measured on 3D printed surfaces although contact angle anisotropy was also observed. This observation is consistent with previous studies that have shown that the surface roughness of the FFF print increases with increasing layer height [18,19]. Overall, the data suggest that the

Table 2
Water contact angles on surfaces with lines printing pattern: effect of raster width

Raster width (mm)	Perpendicular to tool path				
z-layer height (mm)	0.05	0.1	0.15	0.20	0.25
0.2	73.9 ± 2.9	77.5 ± 7.5	72.4 ± 1.6	84.9 ± 3.2	82.0 ± 1.6
0.25	78.6 ± 2.3	75.9 ± 4.5	77.3 ± 1.9	89.0 ± 3.0	88.9 ± 6.3
0.30	75.8 ± 2.5	76.6 ± 4.2	75.6 ± 3.0	78.2 ± 5.0	89.6 ± 7.7
0.35	72.4 ± 2.3	82.2 ± 0.9	90.0 ± 4.2	89.9 ± 2.9	97.7 ± 2.2
0.4	72.9 ± 6.2	89.3 ± 5.8	83.1 ± 2.7	91.9 ± 6.8	105.8 ± 3.3
0.45	90.0 ± 2.2	93.5 ± 3.7	90.3 ± 4.0	95.1 ± 3.1	109.4 ± 6.9
0.50	102.7 ± 2.6	90.7 ± 5.0	92.1 ± 4.9	99.1 ± 5.0	105.8 ± 5.1
0.55	106.7 ± 2.8	94.4 ± 2.2	109.1 ± 5.8	111.1 ± 2.4	113.4 ± 6.8
0.6	122.0 ± 5.2	103.5 ± 4.0	103.8 ± 7.7	111.0 ± 4.1	108.3 ± 2.0
Raster width (mm)	**Parallel to tool path**				
z-layer height (mm)	0.05	0.1	0.15	0.20	0.25
0.2	68.3 ± 7.0	72.2 ± 2.5	75.3 ± 3.3	76.1 ± 4.5	63.3 ± 0.6
0.25	72.3 ± 1.8	70.6 ± 1.5	74.8 ± 7.1	76.3 ± 2.1	75.8 ±5.0
0.30	70.9 ± 0.7	74.4 ± 7.0	73.6 ± 2.4	84.4 ± 3.1	72.5 ± 1.0
0.35	74.2 ± 4.6	79.0 ± 2.3	75.8 ± 1.9	79.2 ± 1.5	84.8 ± 7.7
0.40	84.3 ± 3.0	75.6 ± 3.8	72.9 ± 2.5	75.2 ± 5.3	71.4 ± 5.6
0.45	77.4 ± 6.2	81.8 ± 2.3	74.2 ± 2.3	76.8 ± 11.2	81.2 ± 4.5
0.50	71.3 ± 1.4	74.2 ± 6.4	75.6 ± 2.4	84.8 ± 13.1	81.2 ± 5.5
0.55	76.6 ±4.4	78.2 ± 5.6	75.9 ± 4.1	72.1 ± 5.9	75.0 ± 5.2
0.60	72.1 ± 5.4	76.9 ± 3.4	76.9 ± 1.7	69.3 ± 7.9	77.1 ± 1.8

water contact angle anisotropy (ΔC_A) increases as layer height increases up to around 30 ° at the largest layer heights.

Next, we measured water contact angles on the bottom surface of the 3D printed cubes, i.e. the surface that is in contact with the build platform. When Blu Tape was used to improve adherence to the glass build plate of the Ultimaker 2Go we observed that, both parallel and perpendicular to the tool path, there was no significant variation in the water contact angle. Overall, the values obtained were predominantly consistent with full wetting of PLA, and hence broadly similar to those obtained on the top surface. A significant amount of variation in these water contact angles was observed, which we attribute to the difficulty of obtaining a consistently smooth build surface when the tape is applied. When Kapton Tape was applied to the build platform the water contact angle parallel to the tool path was broadly consistent with the values obtained using Blu Tape and again consistent with full wetting of PLA. Perpendicular to the tool path a trend was observed such that as the z-layer height decreased the water contact angle increased from 91.4 ± 5.3 ° to 112.6 ± 8.1 °. These water contact angles are consistent with partial wetting when the PLA is printed on Kapton Tape and overall significant contact angle anisotropy (ΔC_A is in the region of 10 to 30 °) is observed when using Kapton Tape on the build platform. The trend observed on the bottom surface is opposite to that observed on the top surface. i.e. as the layer height decreases partial wetting is observed, we attribute this to voids left between the extruded filaments, which are likely larger when the layer height is less than the distance between the extruder head and build platform (0.15 mm).

Next, the water contact angles of the outer faces of the sides of the 3D printed cube were evaluated. In principle, build platform levelling and the position of the 3D print on the build platform can impact the deposition of individual layers and the surface roughness, therefore all four faces of the 3D print were measured separately. Table 1 shows that, within error, decreases in the z-layer height do not impact the water contact angle on the side of the print, if measured parallel to the build direction. This trend is observed for each printed face and for the average of all faces, which have a typical contact angle of around 76 °. This value is consistent with full wetting.

When the water contact angles are measured on the sides of the 3D print and perpendicular to the build direction the data in Table 1 show that a significant increase in the water contact angle occurs as the layer height increases. The average values observed range from 92.8 ± 8.8 ° at a layer height of 0.05 mm, to 108.5 ± 4.0 ° at a layer height of 0.25 mm. These values demonstrate anisotropic water contact angle behavior where ΔC_A is in the region of 10 to 20 °, depending on layer height. This is broadly in line with studies that have shown that water contact angles measured parallel and perpendicular to the 3D printed layers are about 72 ° and 105 °, respectively, and the $\Delta C_A > 10$ ° [24], although the effect of layer height was not reported.

3.2. *The effect of raster width on the wettability of 3D printed surfaces*

Table 2 shows the water contact angles on the top surface of the 3D printed cubes measured at raster width intervals of 0.05 mm, from 0.05 to 0.60 mm. It is anticipated that as the raster width exceeds the nozzle diameter (0.4 mm), voids will occur in the 3D printed surface, which will drive reentrant behavior in the water droplet.

In Table 2 a clear trend emerges whereby the water contact angle measured perpendicular to the tool path increases from *circa* 70 ° through > 110 °, as the raster width is increased. This is consistent with full wetting at low raster widths and partial wetting at higher raster widths. This trend of increasing water contact angle occurs at all the z-layer heights measured, although there is quite a lot of variation in the measurements, which is attributed to the variance in the roughness of the surfaces. When water contact angles are measured parallel to the tool path there is no variation in water contact angle within error and all values are consistent with full wetting *circa* 70 to 85 °. Overall, as the raster width is increased the contact angle anisotropy increases up to a value of ΔC_A in the

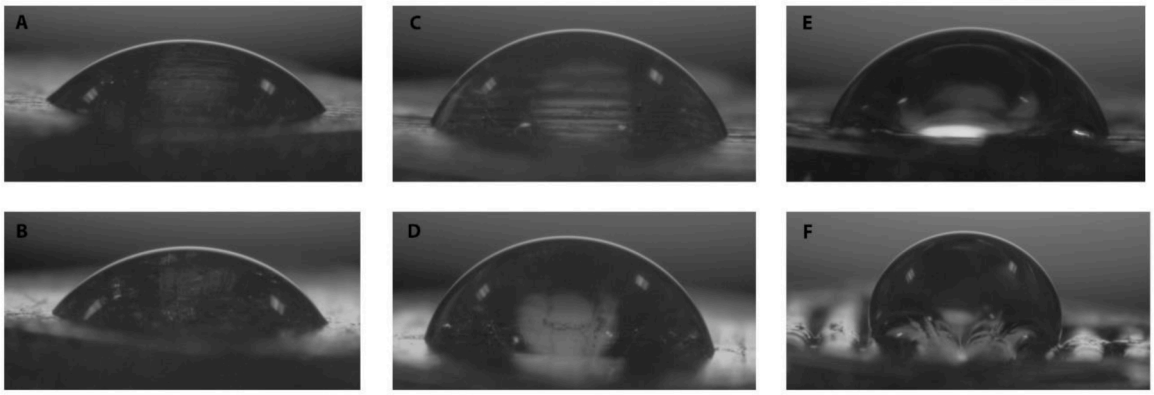

Fig. 3. Example images of the water contact angle on 3D printed surfaces. Fig. 3A and 3B show data obtained at 0.05 mm z-layer height and 0.2 mm raster width, parallel (3A) and perpendicular (3B) orientations. Fig. 3C and 3D show data obtained at 0.10 mm z-layer height and 0.4 mm raster width, parallel (3C) and perpendicular (3D) orientations. Fig. 3E and 3F show data obtained at 0.25 mm z-layer height and 0.6 mm raster width, parallel (3E) and perpendicular (3F) orientations.

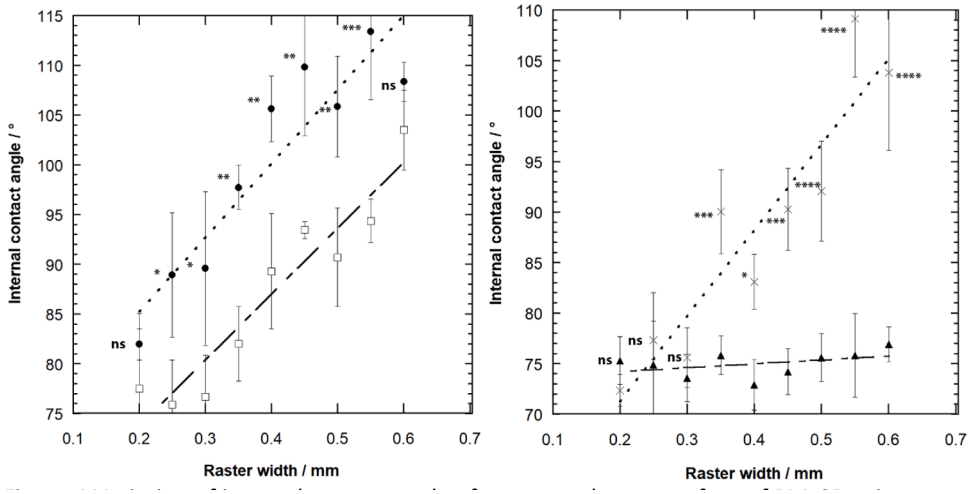

Fig. 4. Variation of internal contact angle of water on the top surface of PLA 3D prints at different raster widths. Fig 4A show data obtained perpendicular to the tool path, where filled circles and empty squares are recorded at z-layer heights of 0.25 and 0.1 mm respectively. Fig. 4B shows data obtained at a z-layer height of 0.15 mm, where crosses and filled triangles are internal contact angles measured perpendicular and parallel to the tool path, respectively. Data are the mean arithmetic average plus or minus the standard deviation of the mean. Data labels show statistical significance defined as ns (not significant), * ($p < 0.05$), ** ($p < 0.01$), *** ($p < 0.001$), **** ($p < 0.0001$). Pairwise comparison, between samples at identical raster widths, were made using a one-way ANOVA analysis with 95% confidence interval. Fig S1 shows the data graphed in an alternative format.

region of > 30 °. Fig. 3 provides example contact angle images, which clearly demonstrate contact angle anisotropy increases as raster width increases. Example data are graphed in Figure 4, which shows the statistical significance of these trends.

Finally, it should be noted that measurement of contact angles enables surface free energy calculations to be performed [43]. The most robust methods make contact angle measurements using multiple different liquids, however a few one liquid probe methods such as the Neumann method have been published [44]. These equation of state methods utilize an empirically derived constant that gives good agreement with other surface free energy calculations, as discussed [43], for low energy surfaces. Given the range of water contact angles we report for the surfaces of 3D prints, and the likely mixture of full wetting and partial wetting at different print settings, we are cautious to report surface free energy values based on these equation of state methods. However the methodology and assumptions are available for the interested reader [44].

4. Conclusions

We have presented measurements of the internal contact angles of water on the surfaces of FFF 3D printed parts. Our data show that

a range of different water contact angles can be achieved by adjusting z-layer height and raster width. Varying these different features results in parallel voids on the 3D printed surface, which gives rise to different degrees of contact angle anisotropy. It should be noted that the rough surfaces and the nature of fused filament fabrication resulted in significant variance between prints. We measured all contact angles in the center of the 3D printed surface, however it may be that one reason for the inter-print variance is an overall variance in surface wettability across the entire print surface. A full study, using a surface area greater than the 1 cm^2 we used will be required to determine this. The high contact angle anisotropies might also account for some of these errors, however we suspect that microscopic variation in the extrusion rates or extrusion volumes/ coupled with errors in the z-axis zero position are the most significant source of these errors. Nonetheless, in general we observed that small z-layer heights (*circa* 0.05 mm) and small raster widths (*circa* 0.2 mm), gave an isotropic contact angle consistent with full wetting of PLA, whilst larger z-layer heights (*circa* 0.25 mm) and larger raster width (*circa* 0.6 mm) resulted in contact angle anisotropy and partial wetting. Furthermore, these contact angle anisotropies were statistically significant, as show in Fig. 4.

These data demonstrate that experimenting with z-layer height and raster width are strategies worth considering for applications where the wettability of the FFF 3D printed part is important. A few examples of relevant applications in the literature are bone tissue engineering [34], and other biomedical applications [34], which build on previous work showing that water contact angle is important for biocompatibility [45]. However, there is growing interest in a wide range of 3D printing applications, such 3D printed electrochemical sensors, produced from conductive filaments [46]. Since the performance of electrochemical sensors and electrochemical storage devices are contact angle dependent [47], FFF might also offer a convenient way to optimize electrode surfaces. Our results might have applications in 3D printed solid catalysis [36] or 3D printed catalytic supports [37] where surface wettability can impact catalytic activity [38] and might be enhanced by different fabrication settings. Finally, these data emphasize the importance of reporting full 3D print settings in scientific publications and suggest that end users should give due consideration to whether, or not, 3D print settings will impact wettability, reproducibility and performance in their chosen application.

Specifications Table

Subject area	*Physical chemistry, biomaterials characterization*
Compounds	*Polylactic acid*
Data category	*Water contact angles*
Data acquisition format	*Image analysis*
Data type	*Analyzed*
Procedure	*Contact angles goniometry*
Data accessibility	*Data in article*

Declaration of Competing Interest

The authors declare that they have no known competing financial interests or personal relationships that could have appeared to influence the work reported in this paper.

Supplementary materials

Supplementary material associated with this article can be found, in the online version, at doi:10.1016/j.cdc.2022.100884.

Appendix. Supplementary Materials

Full list of 3D print settings, supplementary figures

References

[1] P.J. Kitson, S. Glatzel, W. Chen, C.-G. Lin, Y.-F. Song, L. Cronin, 3D printing of versatile reactionware for chemical synthesis, Nat. Protoc. 11 (2016) 920–936, https://doi.org/10.1038/nprot.2016.041.
[2] V. Dragone, V. Sans, M.H. Rosnes, P.J. Kitson, L. Cronin, 3D-printed devices for continuous-flow organic chemistry, Beilstein J. Org. Chem. 9 (2013) 951–959, https://doi.org/10.3762/bjoc.9.109.
[3] P.J. Kitson, R.J. Marshall, D. Long, R.S. Forgan, L. Cronin, 3D Printed High-Throughput Hydrothermal Reactionware for Discovery, Optimization, and Scale-Up, Angew. Chemie Int. Ed. 53 (2014) 12723–12728.
[4] Y. Wei, I. Mayoral-Delgado, N.A. Stewart, M.K. Dymond, Macromolecular crowding and membrane binding proteins: The case of phospholipase A1, Chem. Phys. Lipids. 218 (2019) 91–102, https://doi.org/10.1016/j.chemphyslip.2018.12.006.
[5] J. Pisaruka, M.K. Dymond, A low volume 3D-printed temperature-controllable cuvette for UV visible spectroscopy, Anal. Biochem. 510 (2016) 52–55, https://doi.org/10.1016/j.ab.2016.07.019.
[6] J.M. Brisendine, A.C. Mutter, J.F. Cerda, R.L. Koder, A three-dimensional printed cell for rapid, low-volume spectroelectrochemistry, Anal. Biochem. 439 (2013) 1–3, https://doi.org/10.1016/j.ab.2013.03.036.

[7] Y. Liang, Q. Liu, S. Liu, X. Li, Y. Li, M. Zhang, One-step 3D printed flow cells using single transparent material for flow injection spectrophotometry, Talanta 201 (2019) 460–464, https://doi.org/10.1016/j.talanta.2019.04.009.
[8] M. Michalec, Ł. Tymecki, 3D printed flow-through cuvette insert for UV–Vis spectrophotometric and fluorescence measurements, Talanta 190 (2018) 423–428, https://doi.org/10.1016/j.talanta.2018.08.026.
[9] M. Michalec, R. Koncki, Ł. Tymecki, Optoelectronic detectors for flow analysis systems manufactured by means of rapid prototyping technology, Talanta 198 (2019) 169–178, https://doi.org/10.1016/j.talanta.2019.01.092.
[10] E. Sirjani, M. Migas, P.J. Cragg, M.K. Dymond, 3D printed UV/VIS detection systems constructed from transparent filaments and immobilised enzymes, Addit. Manuf. 33 (2020), 101094, https://doi.org/10.1016/j.addma.2020.101094.
[11] E. Sirjani, Developing protein-based bio-inks for FDM 3D printed microfluidic and millifluidic biosensor applications, University of Brighton, 2019.
[12] S.A.N. Gowers, V.F. Curto, C.A. Seneci, C. Wang, S. Anastasova, P. Vadgama, G.Z. Yang, M.G. Boutelle, 3D Printed Microfluidic Device with Integrated Biosensors for Online Analysis of Subcutaneous Human Microdialysate, Anal. Chem. 87 (2015), https://doi.org/10.1021/acs.analchem.5b01353.
[13] L. Krejcova, L. Nejdl, M.A.M. Rodrigo, M. Zurek, M. Matousek, D. Hynek, O. Zitka, P. Kopel, V. Adam, R. Kizek, 3D printed chip for electrochemical detection of influenza virus labeled with CdS quantum dots, Biosens. Bioelectron. 54 (2014), https://doi.org/10.1016/j.bios.2013.10.031.
[14] E. Sirjani, P.J. Cragg, M.K. Dymond, Glass transition temperatures, melting temperatures, water contact angles and dimensional precision of simple fused deposition model 3D prints and 3D printed channels constructed from a range of commercially available filaments, Chem. Data Collect. 22 (2019), 100244, https://doi.org/10.1016/j.cdc.2019.100244.
[15] J.L. Erkal, A. Selimovic, B.C. Gross, S.Y. Lockwood, E.L. Walton, S. McNamara, R.S. Martin, D.M. Spence, 3D printed microfluidic devices with integrated versatile and reusable electrodes, Lab Chip. 14 (2014), https://doi.org/10.1039/c4lc00171k.
[16] S. Waheed, J.M. Cabot, N.P. Macdonald, T. Lewis, R.M. Guijt, B. Paull, M.C. Breadmore, 3D printed microfluidic devices: enablers and barriers, Lab Chip. 16 (2016), https://doi.org/10.1039/C6LC00284F.
[17] E.J. McCullough, V.K. Yadavalli, Surface modification of fused deposition modeling ABS to enable rapid prototyping of biomedical microdevices, J. Mater. Process. Technol. 213 (2013) 947–954, https://doi.org/10.1016/j.jmatprotec.2012.12.015.
[18] J. Hartcher-O'Brien, J. Evers, E. Tempelman, Surface roughness of 3D printed materials: Comparing physical measurements and human perception, Mater. Today Commun. 19 (2019) 300–305, https://doi.org/10.1016/j.mtcomm.2019.01.008.
[19] M.S. Alsoufi, A.E. Elsayed, Surface Roughness Quality and Dimensional Accuracy—A Comprehensive Analysis of 100% Infill Printed Parts Fabricated by a Personal/Desktop Cost-Effective FDM 3D Printer, Mater. Sci. Appl. 09 (2018) 11–40, https://doi.org/10.4236/msa.2018.91002.
[20] M.S. Alsoufi, A.E. Elsayed, How Surface Roughness Performance of Printed Parts Manufactured by Desktop FDM 3D Printer with PLA+ is Influenced by Measuring Direction, Am. J. Mech. Eng. 5 (2017) 211–222, https://doi.org/10.12691/ajme-5-5-4.
[21] Y. Thomas, An Essay on the cohesion of fluids, Philos. Trans. 95 (1805) 65–87, https://doi.org/10.9772/jpspe1979.17.39.
[22] A. Marmur, Equilibrium contact angles: Theory and measurement, Colloids Surf. A Physicochem. Eng. Asp. 116 (1996) 55–61, https://doi.org/10.1016/0927-7757(96)03585-6.
[23] A. Marmur, Wetting on hydrophobic rough surfaces: To be heterogeneous or not to be? Langmuir 19 (2003) 8343–8348, https://doi.org/10.1021/la0344682.
[24] K.M. Lee, H. Park, J. Kim, D.M. Chun, Fabrication of a superhydrophobic surface using a fused deposition modeling (FDM) 3D printer with poly lactic acid (PLA) filament and dip coating with silica nanoparticles, Appl. Surf. Sci. 467–468 (2019) 979–991, https://doi.org/10.1016/j.apsusc.2018.10.205.
[25] D. Puppi, F. Chiellini, Biodegradable Polymers for Biomedical Additive Manufacturing, Appl. Mater. Today. 20 (2020), 100700, https://doi.org/10.1016/j.apmt.2020.100700.
[26] A. Haryńska, H. Janik, M. Sienkiewicz, B. Mikolaszek, J. Kucińska-Lipka, PLA-Potato Thermoplastic Starch Filament as a Sustainable Alternative to the Conventional PLA Filament: Processing, Characterization, and FFF 3D Printing, ACS Sustain. Chem. Eng. 9 (2021) 6923–6938, https://doi.org/10.1021/acssuschemeng.0c09413.
[27] U. Modi, S. Prakash, Wettability of 3D printed polylactic acid (PLA) parts, AIP Conf. Proc. 2148 (2019) 30052, https://doi.org/10.1063/1.5123974.
[28] M.S. Amirruddin, K.I. Ismail, T.C. Yap, Effect of layer thickness and raster angle on the tribological behavior of 3D printed materials, Mater. Today Proc. 48 (2021) 1821–1825, https://doi.org/10.1016/j.matpr.2021.09.139.
[29] K. Webb, V. Hlady, P.A. Tresco, Relative importance of surface wettability and charged functional groups on NIH 3T3 fibroblast attachment, spreading, and cytoskeletal organization, J. Biomed. Mater. Res. 41 (1998) 422–430.
[30] L. Xu, C.A. Siedlecki, Effects of surface wettability and contact time on protein adhesion to biomaterial surfaces 28 (2007) 3273–3283, https://doi.org/10.1016/j.biomaterials.2007.03.032.
[31] D. da Silva, M. Kaduri, M. Poley, O. Adir, N. Krinsky, J. Shainsky-Roitman, A. Schroeder, Biocompatibility, biodegradation and excretion of polylactic acid (PLA) in medical implants and theranostic systems, Chem. Eng. J. 340 (2018) 9–14, https://doi.org/10.1016/j.cej.2018.01.010.
[32] R.R. Jose, M.J. Rodriquez, T.A. Dixon, F.G. Omenetto, D.L. Kaplan, Evolution of Bioinks and Additive Manufacturing Technologies for 3D Bioprinting, ACS Biomater. Sci. Eng. (2016), https://doi.org/10.1021/acsbiomaterials.6b00088 acsbiomaterials.6b00088.
[33] A. Haryńska, I. Carayon, P. Kosmela, A. Brillowska-Dąbrowska, M. Łapiński, J. Kucińska-Lipka, H. Janik, Processing of polyester-urethane filament and characterization of fff 3d printed elastic porous structures with potential in cancellous bone tissue engineering, Materials (Basel) 13 (2020) 1–22, https://doi.org/10.3390/ma13194457.
[34] A. Haryńska, I. Carayon, P. Kosmela, K. Szeliski, M. Łapiński, M. Pokrywczyńska, J. Kucińska-Lipka, H. Janik, A comprehensive evaluation of flexible FDM/FFF 3D printing filament as a potential material in medical application, Eur. Polym. J. 138 (2020), 109958, https://doi.org/10.1016/j.eurpolymj.2020.109958.
[35] A. Haryńska, J. Kucinska-Lipka, A. Sulowska, I. Gubanska, M. Kostrzewa, H. Janik, Medical-grade PCL based polyurethane system for FDM 3D printing-characterization and fabrication, Materials (Basel) 16 (2019), https://doi.org/10.3390/ma12060887.
[36] C.R. Tubío, J. Azuaje, L. Escalante, A. Coelho, F. Guitián, E. Sotelo, A. Gil, 3D printing of a heterogeneous copper-based catalyst 334 (2016) 110–115, https://doi.org/10.1016/j.jcat.2015.11.019.
[37] I. Pulko, J. Wall, P. Krajnc, N.R. Cameron, Ultra-High Surface Area Functional Porous Polymers by Emulsion Templating and Hypercrosslinking : Efficient Nucleophilic Catalyst Supports (2010) 2350–2354, https://doi.org/10.1002/chem.200903043.
[38] L. Wang, F. Xiao, The Importance of Catalyst Wettability 310028 (2014) 3048–3052, https://doi.org/10.1002/cctc.201402437.
[39] E. Delamarche, D. Juncker, H. Schmid, Microfluidics for Processing Surfaces and Miniaturizing Biological Assays, Adv. Mater. 17 (2005) 2911–2933, https://doi.org/10.1002/adma.200501129.
[40] Y. He, Y. Wu, J.Z. Fu, Q. Gao, J.J. Qiu, Developments of 3D Printing Microfluidics and Applications in Chemistry and Biology: a Review, Electroanalysis 28 (2016), https://doi.org/10.1002/elan.201600043.
[41] J.M. Barrios, P.E. Romero, Improvement of surface roughness and hydrophobicity in PETG parts manufactured via fused deposition modeling (FDM): An application in 3D printed self-cleaning parts, Materials (Basel) 12 (2019), https://doi.org/10.3390/ma12152499.
[42] E. Baran, H. Erbil, Surface Modification of 3D Printed PLA Objects by Fused Deposition Modeling: A Review, Colloids and Interfaces 3 (2019) 43, https://doi.org/10.3390/colloids3020043.
[43] M. Żenkiewicz, Methods for the calculation of surface free energy of solids, J. Achiev. Mater. Manuf. Eng. 24 (2007) 137–145.
[44] D.Y. Kwok, A.W. Neumann, Contact angle measurement and contact angle interpretation, Adv. Colloid Interface Sci. 81 (1999) 167–249, https://doi.org/10.1016/S0001-8686(98)00087-6.
[45] K.L. Menzies, L. Jones, The impact of contact angle on the biocompatibility of biomaterials, Optom. Vis. Sci. Off. Publ. Am. Acad. Optom. 87 (2010) 387–399, https://doi.org/10.1097/OPX.0b013e3181da863e.
[46] H.H. Hamzah, S.A. Shafiee, A. Abdalla, B.A. Patel, 3D printable conductive materials for the fabrication of electrochemical sensors: A mini review, Electrochem. Commun. 96 (2018) 27–31, https://doi.org/10.1016/j.elecom.2018.09.006.
[47] C. Kalinke, P.R. de Oliveira, N.V. Neumsteir, B.F. Henriques, G. de Oliveira Aparecido, H.C. Loureiro, B.C. Janegitz, J.A. Bonacin, Influence of filament aging and conductive additive in 3D printed sensors, Anal. Chim. Acta. 1191 (2022), 339228, https://doi.org/10.1016/j.aca.2021.339228.